Journal of Materials Chemistry A

ROYAL SOCIETY OF CHEMISTRY

PAPER

View Article Online
View Journal | View Issue

Cite this: J. Mater. Chem. A, 2025, 13, 25590

Direct formation of MXene domains and compositional defects in magnetron sputtered V_2AlC-AlO_x heterostructures revealed by theory and experiments†

P. J. Pöllmann, ‡[a] R. Sahu,‡§[ab] M. Fečík, [a] C. Scheu[bc] and J. M. Schneider [ad]

Received 16th February 2025
Accepted 1st July 2025

DOI: 10.1039/d5ta01276g

rsc.li/materials-a

We report on direct formation of nanometer-sized V_2C and novel V_3C_2 MXene domains at V_2AlC-AlO_x heterostructure interfaces synthesized by physical vapor deposition. Their formation is facilitated by local Al deintercalation from V_2AlC MAX phase into AlO_x enabled by the selected architecture maximizing the contact area of V_2AlC MAX phase and AlO_x. Furthermore, the formation of VC, V_3AlC_2, V_5AlC_4, V_7AlC_6, V_8AlC_7, and $V_{10}AlC_9$ compositional defects is observed by aberration-corrected transmission electron microscopy and formation thereof is, together with the MXene formation, rationalized by density functional theory calculations. The applied synthesis approach thus shows the potential to be a step towards the chemical etching-free production of MXenes and can be further extended to other MXene compositions, since the A elements typically have a large affinity to oxygen.

Introduction

Since the discovery of graphene,[1,2] the scientific interest in inorganic two-dimensional (2D) materials has been on the rise and the search for novel compounds is still ongoing. One ever-expanding class of 2D materials are transition metal carbides, nitrides, and carbonitrides – oftentimes collectively called MXenes to emphasize their structural similarity to graphene – where M designates the transition metal and X carbon or nitrogen.[3,4] They are usually prepared by selective wet chemical etching of the A element (referring to III A or IVA elements) from their nanolaminated parent MAX phases, where MX layers are interleaved with A layers, yielding 2D $M_{n+1}X_n$ sheets.[5,6] Bulk MAX phases are typically synthesized at above 1000 °C,[7–9] and are subsequently used as precursors for 2D MXenes.[3,4,8,10] Over 70% of publications describing such synthesis pertain to Ti-based MXenes.[11]

A member of the ternary MAX phases, V_2AlC, has been studied due to its irradiation tolerance[12] and the almost identical electrical resistivity for film thicknesses of 10–50 nm which might be of great potential for future semiconductor applications.[13] Moreover, it has been demonstrated that V_2AlC can be synthesized at temperatures as low as 580 °C employing magnetron sputtering.[14,15]

Etching of V_2AlC with hydrofluoric acid (HF) leads to selective removal of Al and formation of V_2CT_x MXene, which showed high capacity and high cycling rates during testing as electrode materials for lithium-ion batteries.[8] Regarding further MXenes obtained from the V–Al–C system, the synthesis of $V_4C_3T_x$ by chemical etching of V_4AlC_3 MAX phase has been reported.[16–18] To the authors' knowledge, the $V_3C_2T_x$ MXene has been explored only theoretically, even though the calculations found it a promising candidate for synthesis due to the reasonably high exfoliation energy (0.199 eV $Å^{-2}$) obtained for V_3AlC_2.[19] Theoretical investigations also predicted this MXene possesses great potential as an anode material for metal-ion batteries due to its good electrical conductivity and high theoretical storage capacity.[20]

Similar to MAX phases, ternary MAB phases (where B designates boron) also exhibit 2D derivatives known as MBenes, which are analogously synthesized by selective etching of the A element.[21–23] For these materials, a straightforward process for direct synthesis of 2D MoB MBene domains by magnetron sputtering MoAlB, which were found to form in the vicinity of AlO_x (x referring to the varying molar content of oxygen within the Al–O regions) regions at grain boundaries, was reported.[24–26] It was suggested that these AlO_x regions are formed by oxygen

[a]Materials Chemistry, RWTH Aachen University, Aachen, Germany. E-mail: poellmann@mch.rwth-aachen.de
[b]Max Planck Institute for Sustainable Materials GmbH, Group Nanoanalytics and Interfaces, Düsseldorf, Germany
[c]Materials Analytics, RWTH Aachen University, Aachen, Germany
[d]Max Planck Institute for Sustainable Materials GmbH, Department Structure and Nano-/Micromechanics of Materials, Group Thin Films Materials Design, Düsseldorf, Germany

† Electronic supplementary information (ESI) available. See DOI: https://doi.org/10.1039/d5ta01276g

‡ These authors contributed equally to the publication.

§ Now at: Institute of Nanotechnology, Karlsruhe Institute of Technology, Hermann-von-Helmholtz-Platz 1, 76344 Eggenstein-Leopoldshafen, Germany.

incorporation during deposition and that they facilitate local deintercalation of Al from MoAlB, leading to the formation of nanometer-sized MBene domains without chemical etching.

As several MXenes have been previously reported within the V–Al–C system,[8,16–18] we investigate the formation of MXenes in the vicinity of AlO_x regions,[24–26] capitalizing on the previously identified Al-deintercalation tendency into AlO_x regions, by maximizing the AlO_x-MAX phase contact area through design of a multilayer architecture and the introduction of AlO_x layers during growth. We show the direct formation of V_2CT_x and $V_3C_2T_x$ MXene domains in direct current magnetron sputtered (DCMS) thin films, demonstrating the potential of the proposed novel architecture without employing chemical etching. We furthermore report on several new MAX phase compositional defects and rationalize their formation based on density functional theory (DFT) calculations.

Experimental

Thin film synthesis and analysis

V_2AlC-AlO_x heterostructures have been synthesized by direct current magnetron sputtering (DCMS) in a laboratory-scale high-vacuum physical vapor deposition (PVD) chamber using a ternary 2″ V_2AlC target (Plansee Composite Materials GmbH, Germany) which was operated at 200 W and sequentially opening the O_2 gas flow after every 6 min for 2 min during the sputtering. The target was facing the single-crystalline 10 × 10 mm MgO (001) substrates at a distance of 10 cm. The substrates were kept at floating potential and a temperature of 580 °C at the base pressure of 1.6×10^{-6} mbar while the Ar deposition pressure of 0.5 Pa along with the deposition time of 60 min led to a film thickness of about 1.2 μm.

High-resolution scanning transmission electron microscopy (HRSTEM)

Scanning transmission electron microscopy (STEM) analysis was conducted utilizing a probe-corrected ThermoFisher Titan Themis at an accelerating voltage of 300 kV. Microstructural characterizations were carried out using cross sectional samples. STEM samples were prepared and thinned to below 30 nm by conventional mechanical polishing and Ar ion milling in Gatan PIPS. A semi-convergence angle of 23.8 mrad was selected for high-resolution (HR) STEM imaging. Semi-collection angles ranging from 78–200 mrad and 24–96 mrad were employed for high angle annular dark field (HAADF) and annular dark field (ADF) STEM, respectively. The microscope was equipped with a Bruker SuperX detector for energy-dispersive X-ray spectroscopy (EDX) analysis.

Density functional theory (DFT)

All periodic density functional (DFT) calculations were performed using Quantum ESPRESSO (QE)[27,28] in version 7.2. Electron exchange and correlation were described *via* the generalized gradient approximation (GGA) functional as parametrized by Perdew, Burke, Ernzerhof (PBE).[29] All elements within the investigated structures were described by pseudopotentials provided in Standard solid-state pseudopotentials (SSSP) PBE Precision package[30] in version 1.3.0. To account for the van der Waals interactions, Grimme's D3 correction[31] was employed utilizing damping proposed by Becke and Johnson.[32–34] All the calculations were facilitated by use of the Atomic Simulation Environment (ASE)[35] with employing the slightly modified extension XEspresso[36] allowing to properly handle QE input and output files.

Based on performed convergence tests for MAX structures, we chose 45 Ry and 360 Ry as the kinetic cutoff for wavefunctions and charge density, respectively. For bulk structures of the constituting elements – fcc Al, fcc C and bcc V – the cutoff values were taken directly from the SSSP PBE Precision v1.3.0,[30] cutoff tables: 30/240 Ry for Al, 45/360 Ry for C and 40/320 Ry for V. Convergence thresholds were set to 10^{-5} Ry and 10^{-4} Ry/Bohr for the total energy and forces, respectively. Brillouin zone was sampled by Γ-centered Monkhorst–Pack grid[37] with *k*-points spacing of 0.2 $Å^{-1}$. Vacuum thickness along the *z*-axis for MX structures was chosen as 12 Å. All calculations herein were performed without consideration of spin polarization. Information about the models used and their creation, together with additional information about the calculation's settings, can be found in the ESI Fig. S1 and S2.†

All initial structures were first subjected to geometry optimization allowing their unit cells to change volume as well as shape. For MX structures, *z*-direction of the unit cell was kept fixed. During the optimization, Gaussian smearing with a spread of 0.01 Ry was used. This yielded lattice parameters shown in ESI Table S3.† No changes in space groups during the optimizations were observed. Obtaining the ground state geometries, the structures underwent additional single point calculation utilizing the optimized tetrahedron method[38] to obtain accurate total energies. These were then used to calculate the energies of formation E_f of MAX phases against their constituting elements at 0 K following the equation

$$E_f = \frac{E_{TOT}^{MAX}}{N} - \sum_i x_i \frac{E_{TOT}^{i}}{n_i}, \quad (1)$$

where the summation goes over the constituting elements – i = V, Al, C (i = V, C) for the MAX (MX) case, N is a number of formula units per the unit cell, x_i is a stoichiometric coefficient of an element i, and n_i is the total number of atoms within a bulk system of an element i.

Results and discussion

Following the herein proposed architecture, a heterostructure has been synthesized and its multilayered nature is readily visible in the low magnification HAADF STEM micrographs in Fig. 1a. The dark grey regions consist of AlO_x (yellow arrows) whereas the brightest regions are identified as V_2AlC MAX phase (white arrows), as the intensity (I) is roughly proportional to Z^2 (Z referring to the atomic number).[39] The V_2AlC layers on the MgO substrate exhibit narrow, randomly oriented grains with small pores visible as dark spots (red arrows) in the HAADF micrographs while the AlO_x layers show a defined and

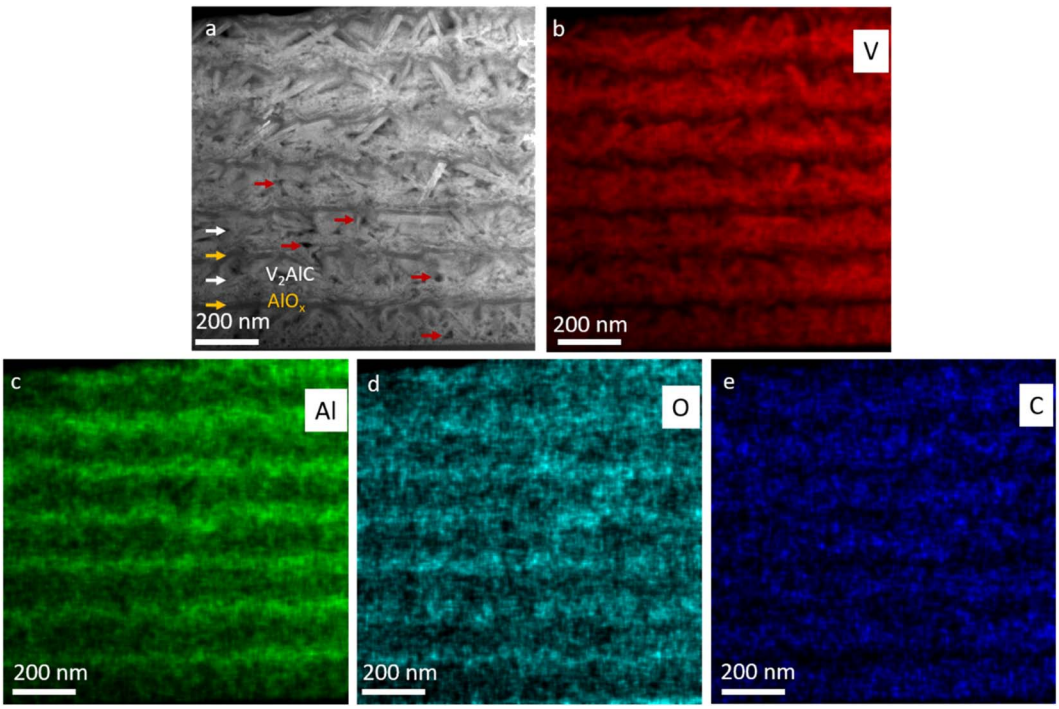

Fig. 1 (a) Overview of V_2AlC-AlO_x multilayer thin film in cross sectional HAADF STEM image. A section of the film reveals chemical composition of V, Al, C and O in STEM EDX maps (b–e).

continuous microstructure (Fig. 1a). The average length and width of the grains are in a range of approximately 70 to 150 nm and 15 to 40 nm, respectively. Along with X-ray diffraction, fast Fourier transformations (FFTs) of the HAADF images confirm the presence of V_2AlC MAX phase with lattice parameters $a = 2.8 \pm 0.1$ Å and $c = 13.5 \pm 0.2$ Å (see ESI Fig. S4 and S5†). This is in good agreement to the values predicted by DFT (ESI S3†) with a difference of around 3% for both a and c parameters. Pore sizes vary between approximately 10 to 40 nm. The chemical composition was measured by EDX and the corresponding compositional maps of the constituting elements (V, Al, C, and O) are shown in Fig. 1b–e. It is evident from the STEM EDX maps, that V and C are uniformly distributed and constrained to the V_2AlC layers, while Al and O are distributed over the whole sample with their highest proportion in the AlO_x layers (Fig. 1b–e). This preferential Al distribution is a first indication of Al deintercalation from the MAX phase into AlO_x. The selective removal of Al from the $V_{n+1}AlC_n$ structure can be rationalized based on the Al bonding: metallic V–Al bonds in the MAX phase are with a calculated bond energy of 1.09 eV significantly weaker compared to the covalent/ionic V–C bonds with 2.77 eV.[40] Hence, Al is the most weakly bound species within the phase, facilitating its deintercalation. The presence of oxygen within the V_2AlC layers might result from residual gas incorporation during the deposition process or might be surface oxide formed after lamellae preparation.[41,42]

In Fig. 2, the formation of 2D derivatives of vanadium-based MAX phases is observed in the HAADF HRSTEM micrographs for a domain adjacent to an AlO_x region. A delaminated region, serving as evidence of a 2D phase, is indicated by white arrows, see Fig. 2a. A higher magnification of the region marked with a dotted rectangle in Fig. 2a is shown in Fig. 2b.

The atomic columns of V are visible as bright dots, while Al columns appear dark grey in the HAADF HRSTEM micrograph. Due to their low scattering amplitude, the significantly lighter elements C and O are invisible in the micrograph. A representative overlay identifying individual atomic columns (here and throughout the text: V as red, Al green, and C as blue) is shown in Fig. 2c as a guide for the eye for easier distinction of individual phases.

Fig. 2b reveals an Al-deprived region in the proximity of the AlO_x regime that further indicates the effectiveness of the applied architecture for Al deintercalation. This region (grey dotted rectangle) is shown in a higher magnification in Fig. 2c revealing a variation in the interlayer distance to the nearest-neighbor $V_{n+1}C_n$ subunit as indicated by the ideal structural overlay. These modulations in distance lead to a layer bending of the $V_{n+1}C_n$ subunits in the vicinity of AlO_x regions. While in pristine V_2AlC regions the projected in-plane distance between the V_2C subunits is 2.51 Å (blue dotted distance markers in Fig. 2e), the distances in the bent regions varies between 2 ± 0.1 Å (purple) and 3.2 ± 0.15 Å (white), resulting in relative differences of −23% and +24% compared to the pristine V_2AlC regions, respectively. The relative differences for V_3C_2 subunits are 1.7 ± 0.1 Å (−32%) and 5.2 ± 0.1 Å (+105%) compared to the projected distance for V_3C_2 subunits in pristine V_3AlC_2 (2.5 Å). This is consistent with our previous observations for structurally similar MBene domains formed in MoAlB MAB phase,[24–26] and indicates local formation of V_2CT_x as well as $V_3C_2T_x$ MXene domains. The areal fraction of MXene domains relative to all

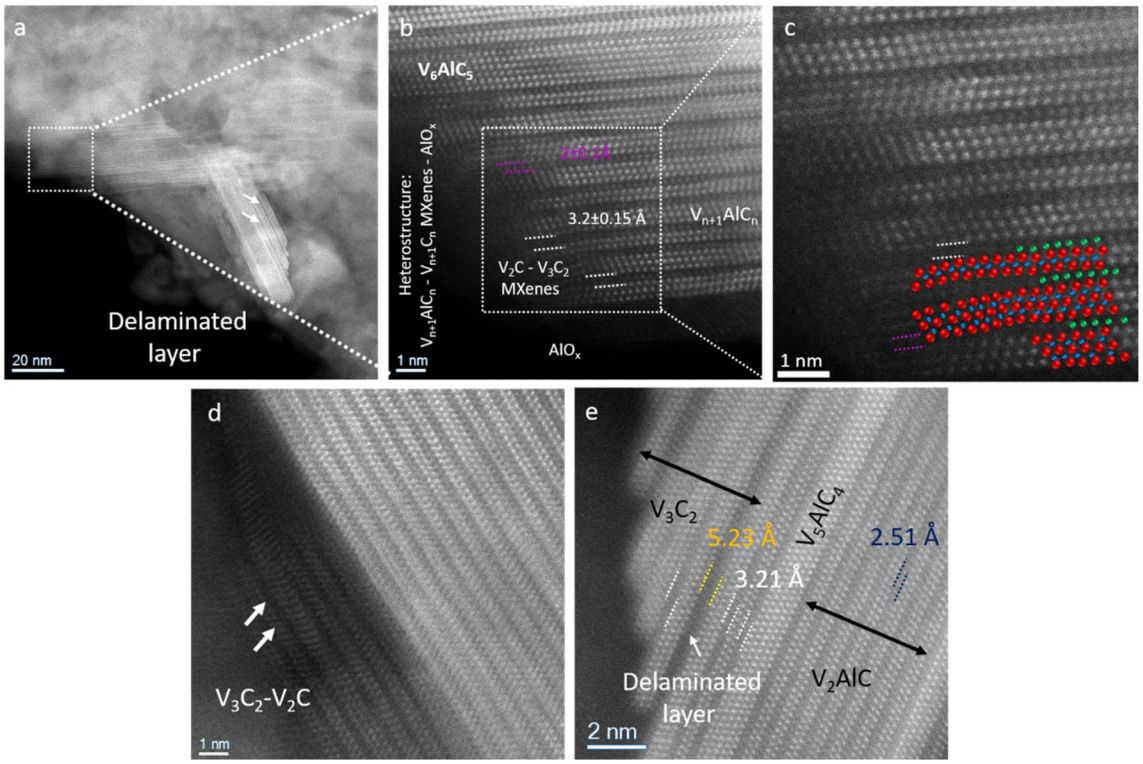

Fig. 2 HAADF STEM micrographs showing formation of V_2CT_x and $V_3C_2T_x$ MXene domains (a–e) including representative overlays of V (red), Al (green), C (blue) atomic positions as a guide for the eye. Al delaminated 2D MXene layers are identified by white arrows in (a) and (d).

other phases is estimated to be close to 1% as determined by high-resolution analysis, whereas the areal fraction determined for the MBene was <1%.[25]

Layer bending characteristic for V_2CT_x and $V_3C_2T_x$ MXene domains can also be observed in other regions of the film in Fig. 2d, while the HRSTEM micrograph in Fig. 2e reveals a delaminated layer of a $V_3C_2T_x$ MXene derivative. The delaminated layer can be clearly identified by the measured projected distance of 5.23 Å (dotted orange distance markers). V_2CT_x MXene has been previously reported experimentally,[8] however, the formation of $V_3C_2T_x$ MXene has not been reported to date. It has, nonetheless, been studied by computational methods predicting it to be a promising candidate for synthesis due to the reasonably low exfoliation energy of V_3AlC_2 of around 2.9 eV (3.0 eV for V_2C);[19,43] hence, supporting the here observed experimental formation. It is also in good agreement with deintercalation barriers (E_d) to form $V_{n+1}C_nT_x$ MXenes from the corresponding $V_{n+1}AlC_n$ ($n = 1$–9) phases calculated herein (see ESI S6†). The deintercalation barriers for all compositions were found to be around 3.5 eV, and therefore in a regime which can be overcome in the employed synthesis scenario, as has been shown for structurally similar MBenes.[24–26] However, it needs to be noted that the calculations were performed at 0 K and without taking any kinetic effects into account, both of which will influence final height of the barriers. The difference of approximately 0.5 eV to the values reported previously for $V_{n+1}C_n$[19,43] arises from the inclusion of van-der-Waals interactions to the calculations performed herein.

The observed formation of V_2CT_x and $V_3C_2T_x$ MXene domains, as opposed to hypothetical $V_{n+1}C_nT_x$ MXenes for $n > 2$, can be rationalized considering the present phase population: since mostly V_2AlC and V_3AlC_2 are observed in the sample, as shown further in Fig. 3, the feasibility of MXene formation *via* Al deintercalation is the highest for these compositions, owing to the fact that deintercalation barriers are similar for all n (ESI S6†).

The detected formation of V_2CT_x and $V_3C_2T_x$ MXene domains shows the potential of the employed synthesis approach. Since during magnetron sputtering the environmental conditions can be precisely modulated, it might be feasible to tune surface terminations of MXenes during synthesis. Furthermore, the synthesis approach is not limited to the current V–Al–C MAX phase system, since a wide range of MAX phases has been previously synthesized using PVD processes.[15,44] Synthesis of these MXene domains also yields potential for their application in metal-ion batteries as stated above.[8,20]

Moreover, two novel MAX phase compositions, V_5AlC_4 and V_6AlC_5, are observed in Fig. 2b (zoomed in from grey dotted square in Fig. 2a) and e, respectively.

The HAADF STEM micrograph in Fig. 3a shows a defective grain of V_2AlC MAX phase adjacent to an amorphous AlO_x region. A chemical composition analysis by a STEM EDX mapping is provided in the ESI S7.† The HRSTEM image taken from the region specified in Fig. 3a at the grain boundary (dotted grey square) is displayed in Fig. 3b. The atomic arrangement of the

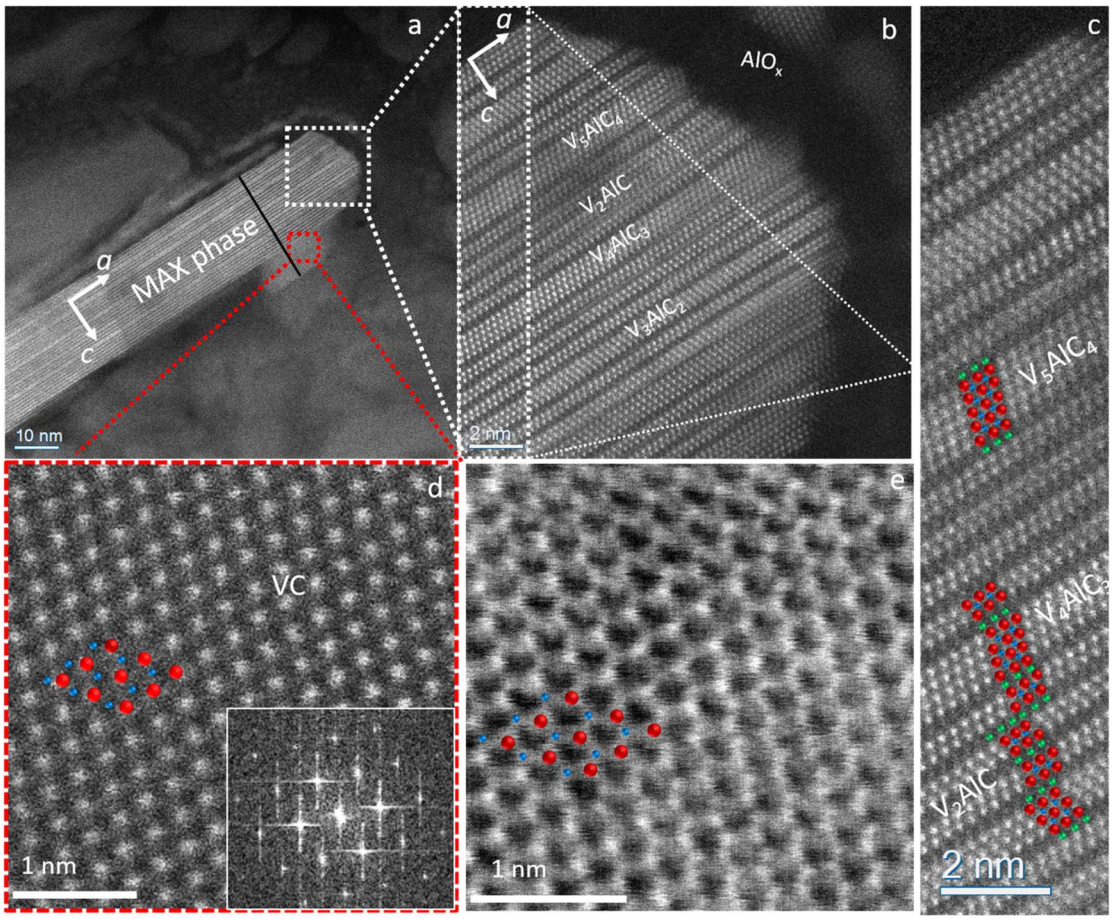

Fig. 3 HAADF STEM micrographs of a defective V_2AlC grain showing formation of multiple low order compositional defects (a–e) including representative overlays of V (red) –Al (green) –C (blue) atomic positions as a guide for the eye. (e) ADF STEM image showing hexagonal atomic arrangement of 3D VC phase acquired from the region marked in the HRSTEM image in (d).

V_2AlC MAX phase, as well as various compositional defect phases, are visible along the [100] zone axis.

While the expected composition of the MAX phase would be solely the 211-type V_2AlC due to the sputter target composition, various Al-deficient compositional defect phases including V_3AlC_2, V_4AlC_3, V_5AlC_4, and V_6AlC_5 are observed additionally (Fig. 2b, e and 3b–d). Among the various compositional defects, V_3AlC_2 exhibits increased density within the thin film – we have observed the formation up to a few layers of this phase (see ESI S8†). While V_4AlC_3 has been reported experimentally,[45,46] and has even been shown to be a precursor for $V_4C_3T_x$ MXene synthesis,[16–18,47] the formation of V_3AlC_2 and V_5AlC_4 have not yet been reported experimentally to date. For V_3AlC_2, first-principles studies have been carried out predicting higher bulk and Young's moduli in comparison to Ti_3AlC_2.[48,49] In case of V_5AlC_4, there is no literature data available. Hence, we employed DFT calculations to obtain energies of formation E_f for $V_{n+1}AlC_n$ (n = 1–9) phases – the results are summarized in Fig. 4 and S9.† As can be readily seen, all studied compositions exhibit negative energies of formation indicating thermodynamic stability for all phases compared to the constituting elements. Consequently, the concurrent (defect) phase formation of $V_{n+1}AlC_n$ exhibited in Fig. 3 (and Fig. 2b) can be rationalized based on both the energies of formation as well as local variations in the surface chemical composition during growth.

It has to be noted though, that the calculations (Fig. 4 and S9†) pertain to 0 K and that competing phases are not considered. Upon consideration of competing phases utilizing previous reports, the 211 and 312 type exhibit a negative enthalpy of formation of −0.072 eV per atom and −0.005 eV per atom while V_4AlC_3 is with 0.006 eV per atom metastable.[50] However, due to the kinetically limited nature of the employed PVD synthesis, formation of V_4AlC_3 is also expected here, as has been shown before for structurally similar MAB phases.[24,25,51]

A rough estimation of the fractions of the described defect phases is conducted by measuring the maximum number of intersection points of the compositional defects (CD) within a given length inside a defective V_2AlC MAX phase grain, yielding a defect population density. Exemplarily for V_5AlC_4, the estimation of the defect phase population within the given grain is computed to be ~0.056 nm^{-1} along the 25 nm black line shown in Fig. 3a. Similar measurements were carried out for all defect phase compositions yielding average populations of 0.44, 0.18, and 0.038 nm^{-1} for the V_2AlC, V_4AlC_3, and V_3AlC_2 phases within the defective V_2AlC matrix, respectively.

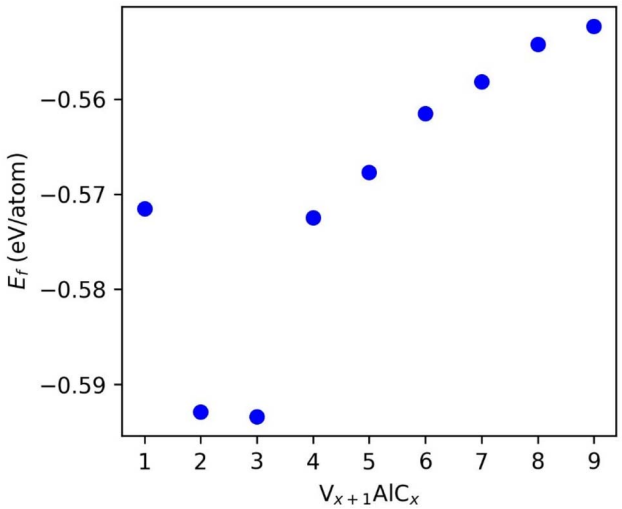

Fig. 4 Energies of formation (E_f) obtained *via* DFT calculations for $V_{n+1}AlC_n$ (n = 1–9) compositions at 0 K.

The effectiveness of the employed layer architecture for localized Al deintercalation is demonstrated by the fact that a 3D crystal of VC, completely deprived of Al, is formed (red dotted rectangle, Fig. 3a). The HAADF STEM micrograph of this region (Fig. 3d) reveals the concurrent formation of V_2AlC and VC phases. To reveal the exact lattice positions of C atoms within the VC phase, ADF STEM imaging, a well-recognized technique for light atom detection,[52] was performed and is shown in Fig. 3e. Combining observations of both HAADF and ADF STEM imaging, a honeycomb crystal structure of the VC phase is evident. Similar images from other regions of the film are available in the ESI S10.†

A further MAX phase grain nestled within an AlO_x region is shown in the HAADF HRSTEM micrograph in Fig. 5a, along with higher magnified regions in Fig. 5b, c and the overlay of the ideal structure similar to Fig. 3. Chemical composition analysis using STEM EDX mapping is provided as evidence of the coexistence of MAX-AlO_x regions, see ESI S7.† As can be seen in Fig. 5b and c, multiple compositional defect phases including V_4AlC_3, V_7AlC_6, V_8AlC_7, and $V_{10}AlC_9$ can be observed in addition

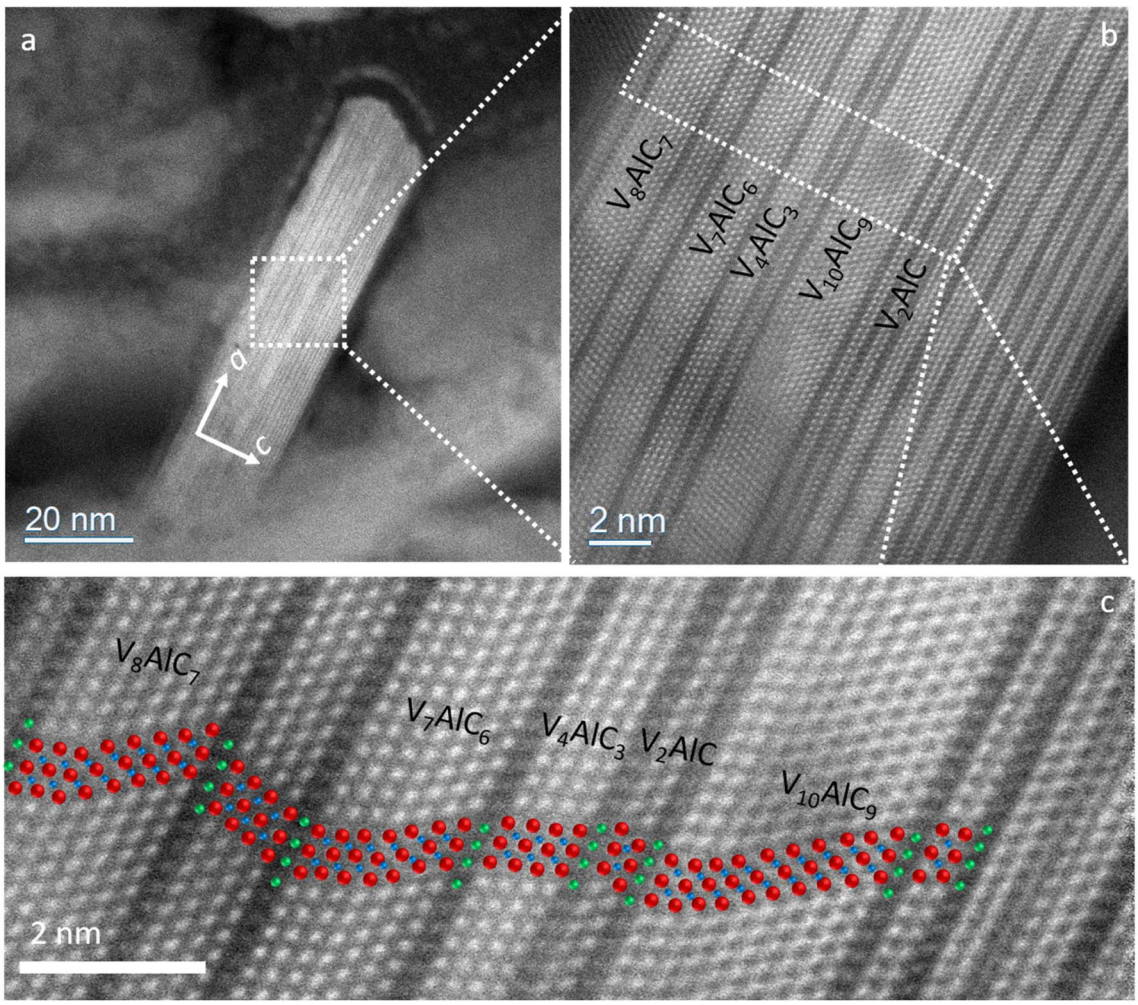

Fig. 5 HAADF HRSTEM micrographs of a defective V_2AlC grain showing formation of multiple high order compositional defects (a–c) including representative overlays of V (red) –Al (green) –C (blue) atomic positions as a guide for the eye.

to the expected V_2AlC. Their presence can be explained by the DFT-predicted energies of formation which are very close to V_2AlC, suggesting all these defect phases can be readily formed. The energetic difference between individual phases, was found to be very small (approximately 41 meV per atom between V_4AlC_3 and $V_{10}AlC_9$ pertaining to the highest difference), and thus can be easily overcome in a metastable synthesis scenario as the one employed here. This has been shown by the synthesis of metastable TiAlN by magnetron sputtering, for which energetic barriers of 123–181 meV per atom have been predicted[53] as well as for compositional defects in sputtered MoAlB MAB phase, with a maximum barrier of formation of 40 meV per atom.[26] Thus, the formation of all observed $V_{n+1}AlC_n$ compositions can be rationalized based on their similar energies of formation and the kinetically limited synthesis scenario employed here.

To the best of our knowledge, this is the first report of novel compositions V_7AlC_6, V_8AlC_7, and $V_{10}AlC_9$, which – together with V_3AlC_2,V_5AlC_4, and V_6AlC_5 shown in Fig. 2 and 3 – extend the known MAX phase family, and show the effectiveness of local Al deintercalation by the employed multilayered architecture.

As has been shown above, MXenes can be readily formed utilizing the chemically activated deintercalation of Al from the parent MAX phase structure. Thus, this synthesis approach is not limited to specific $M_{n+1}AX_n$ phases and can potentially be used to obtain other novel MXene compositions. Furthermore, it can be envisioned that, by precisely tailoring the chemical composition to the desired MAX structure, and employing less energetic deposition conditions, the formation of larger areas thereof could be facilitated and thus leading to preferential formation of the corresponding MXene configuration.

Conclusions

A novel architecture based on providing an interface area between V_2AlC MAX phase and AlO_x regions has been employed during direct current magnetron sputtering thereof. It was demonstrated that the resulting multilayered structure efficiently locally deintercalated Al from the MAX phase leading to formation of multiple hitherto unreported $V_{n+1}AlC_n$ compositional defect phases including V_3AlC_2, V_5AlC_4, V_6AlC_5, V_7AlC_6, V_8AlC_7, and $V_{10}AlC_9$. Moreover, successful synthesis of V_2CT_x and $V_3C_2T_x$ MXene domains was demonstrated using HRSTEM, and formation thereof was rationalized by DFT calculations. Further investigations on the exact nature of surface terminations of the reported MXene domains are encouraged. Moreover, the utilization of PVD for synthesis would potentially allow for the precise tuning of these terminations and is not limited to the V–Al–C material system studied here. The herein introduced synthesis approach thus shows the potential to be a step towards the chemical etching-free production of MXenes.

Data availability

The data supporting this article have been included as part of the ESI.†

Conflicts of interest

The authors declare no competing financial interests.

Acknowledgements

The authors gratefully acknowledge the computing time provided to them at the NHR Center NHR4CES at RWTH Aachen University (project number p0020883). This is funded by the Federal Ministry of Education and Research, and the state governments participating on the basis of the resolutions of the GWK for national high performance computing at universities (www.nhr-verein.de/unsere-partner).

References

1 K. S. Novoselov, A. K. Geim, S. V. Morozov, D. Jiang, Y. Zhang, S. V. Dubonos, *et al.*, Electric Field Effect in Atomically Thin Carbon Films, *Science*, 2004, **306**(5696), 666–669.
2 K. S. Novoselov, D. Jiang, F. Schedin, T. J. Booth, V. V. Khotkevich, S. V. Morozov, *et al.*, Two-dimensional atomic crystals, *Proc. Natl. Acad. Sci. U. S. A.*, 2005, **102**(30), 10451–10453.
3 M. Naguib, M. Kurtoglu, V. Presser, J. Lu, J. J. Niu, M. Heon, *et al.*, Two-Dimensional Nanocrystals Produced by Exfoliation of Ti_3AlC_2, *Adv. Mater.*, 2011, **23**(37), 4248–4253.
4 M. Naguib, O. Mashtalir, J. Carle, V. Presser, J. Lu, L. Hultman, *et al.*, Two-Dimensional Transition Metal Carbides, *ACS Nano*, 2012, **6**(2), 1322–1331.
5 K. R. G. Lim, M. Shekhirev, B. C. Wyatt, B. Anasori, Y. Gogotsi and Z. W. Seh, Fundamentals of MXene synthesis, *Nat. Synth.*, 2022, **1**(8), 601–614.
6 M. W. Barsoum, *MAX Phases: Properties of Machinable Ternary Carbides and Nitrides*, Wiley-VCH, Weinheim, 2013.
7 J. C. Schuster, H. Nowotny and C. Vaccaro, The ternary systems: CrAlC, VAlC, and TiAlC and the behavior of H-phases (M2AlC), *J. Solid State Chem.*, 1980, **32**(2), 213–219.
8 M. Naguib, J. Halim, J. Lu, K. M. Cook, L. Hultman, Y. Gogotsi, *et al.*, New Two-Dimensional Niobium and Vanadium Carbides as Promising Materials for Li-Ion Batteries, *J. Am. Chem. Soc.*, 2013, **135**(43), 15966–15969.
9 S. R. Kulkarni, M. Merlini, N. Phatak, S. K. Saxena, G. Artioli, S. Gupta, *et al.*, High-Temperature Thermal Expansion and Stability of V2AlC Up To 950 °C, *J. Am. Ceram. Soc.*, 2007, **90**(9), 3013–3016.
10 M. Naguib and Y. Gogotsi, Synthesis of Two-Dimensional Materials by Selective Extraction, *Acc. Chem. Res.*, 2015, **48**(1), 128–135.
11 C. Lamiel, I. Hussain, J. H. Warner and K. Zhang, Beyond Ti-based MXenes: A review of emerging non-Ti based metal-MXene structure, properties, and applications, *Mater. Today*, 2023, **63**, 313–338.
12 C. Wang, T. Yang, J. Xiao, S. Liu, J. Xue, Q. Huang, *et al.*, Structural Transitions Induced by Ion Irradiation in V2AlC and Cr2AlC, *J. Am. Ceram. Soc.*, 2016, **99**(5), 1769–1777.
13 J. E. Yoo, J. Y. Sung, J. H. Hwang, I. Maeng, S.-J. Oh, I. Lee, *et al.*, MAX-Phase Films Overcome Scaling Limitations to

the Resistivity of Metal Thin Films, *ACS Appl. Mater. Interfaces*, 2021, **13**(51), 61809–61817.
14 J. M. Schneider, R. Mertens and D. Music, Structure of V2AlC studied by theory and experiment, *J. Appl. Phys.*, 2006, **99**(1), 013501.
15 C. Azina, S. Mráz, G. Greczynski, M. Hans, D. Primetzhofer, J. M. Schneider, *et al.*, Oxidation behaviour of V2AlC MAX phase coatings, *J. Eur. Ceram. Soc.*, 2020, **40**(13), 4436–4444.
16 M. H. Tran, T. Schäfer, A. Shahraei, M. Dürrschnabel, L. Molina-Luna, U. I. Kramm, *et al.*, Adding a New Member to the MXene Family: Synthesis, Structure, and Electrocatalytic Activity for the Hydrogen Evolution Reaction of V4C3T_x, *ACS Appl. Energy Mater.*, 2018, **1**(8), 3908–3914.
17 J. Zhou, S. Lin, Y. Huang, P. Tong, B. Zhao, X. Zhu, *et al.*, Synthesis and lithium ion storage performance of two-dimensional V4C3 MXene, *Chem. Eng. J.*, 2019, **373**, 203–212.
18 X. Wang, S. Lin, H. Tong, Y. Huang, P. Tong, B. Zhao, *et al.*, Two-dimensional V4C3 MXene as high performance electrode materials for supercapacitors, *Electrochim. Acta*, 2019, **307**, 414–421.
19 M. Khazaei, A. Ranjbar, K. Esfarjani, D. Bogdanovski, R. Dronskowski and S. Yunoki, Insights into exfoliation possibility of MAX phases to MXenes, *Phys. Chem. Chem. Phys.*, 2018, **20**(13), 8579–8592.
20 K. Fan, Y. Ying, X. Li, X. Luo and H. Huang, Theoretical Investigation of V3C2 MXene as Prospective High-Capacity Anode Material for Metal-Ion (Li, Na, K, and Ca) Batteries, *J. Phys. Chem. C*, 2019, **123**(30), 18207–18214.
21 L. T. Alameda, R. W. Lord, J. A. Barr, P. Moradifar, Z. P. Metzger, B. C. Steimle, *et al.*, Multi-Step Topochemical Pathway to Metastable Mo2AlB2 and Related Two-Dimensional Nanosheet Heterostructures, *J. Am. Chem. Soc.*, 2019, **141**(27), 10852–10861.
22 L. T. Alameda, P. Moradifar, Z. P. Metzger, N. Alem and R. E. Schaak, Topochemical Deintercalation of Al from MoAlB: Stepwise Etching Pathway, Layered Intergrowth Structures, and Two-Dimensional MBene, *J. Am. Chem. Soc.*, 2018, **140**(28), 8833–8840.
23 V. G. Nair, M. Birowska, D. Bury, M. Jakubczak, A. Rosenkranz and A. M. Jastrzębska, 2D MBenes: A Novel Member in the Flatland, *Adv. Mater.*, 2022, **34**(23), 2108840.
24 R. Sahu, D. Bogdanovski, J.-O. Achenbach, J. M. Schneider and C. Scheu, Defects in an orthorhombic MoAlB MAB phase thin film grown at moderate synthesis temperature, *Nanoscale*, 2022, **14**(7), 2578–2585.
25 R. Sahu, D. Bogdanovski, J. O. Achenbach, S. Y. Zhang, M. Hans, D. Primetzhofer, *et al.*, Direct MoB MBene domain formation in magnetron sputtered MoAlB thin films, *Nanoscale*, 2021, **13**(43), 18077–18083.
26 R. Sahu, D. Bogdanovski, J.-O. Achenbach, M. Hans, D. Primetzhofer, J. M. Schneider, *et al.*, Compositional defects in a MoAlB MAB phase thin film grown by high-power pulsed magnetron sputtering, *Nanoscale*, 2023, **15**(43), 17356–17363.
27 P. Giannozzi, O. Andreussi, T. Brumme, O. Bunau, M. Buongiorno Nardelli, M. Calandra, *et al.*, Advanced capabilities for materials modelling with Quantum ESPRESSO, *J. Phys.: Condens. Matter*, 2017, **29**(46), 465901.
28 P. Giannozzi, S. Baroni, N. Bonini, M. Calandra, R. Car, C. Cavazzoni, *et al.*, QUANTUM ESPRESSO: a modular and open-source software project for quantum simulations of materials, *J. Phys.: Condens. Matter*, 2009, **21**(39), 395502.
29 J. P. Perdew, K. Burke and M. Ernzerhof, Generalized Gradient Approximation Made Simple, *Phys. Rev. Lett.*, 1996, **77**(18), 3865–3868.
30 G. Prandini, A. Marrazzo, I. E. Castelli, N. Mounet and N. Marzari, Precision and efficiency in solid-state pseudopotential calculations, *npj Comput. Mater.*, 2018, **4**(1), 72.
31 S. Grimme, J. Antony, S. Ehrlich and H. Krieg, A consistent and accurate *ab initio* parametrization of density functional dispersion correction (DFT-D) for the 94 elements H-Pu, *J. Chem. Phys.*, 2010, **132**(15), 154104.
32 A. D. Becke and E. R. Johnson, A density-functional model of the dispersion interaction, *J. Chem. Phys.*, 2005, **123**(15), 154101.
33 E. R. Johnson and A. D. Becke, A post-Hartree–Fock model of intermolecular interactions, *J. Chem. Phys.*, 2005, **123**(2), 024101.
34 E. R. Johnson and A. D. Becke, A post-Hartree-Fock model of intermolecular interactions: Inclusion of higher-order corrections, *J. Chem. Phys.*, 2006, **124**(17), 174104.
35 A. Hjorth Larsen, J. Jørgen Mortensen, J. Blomqvist, I. E. Castelli, R. Christensen, M. Dułak, *et al.*, The atomic simulation environment—a Python library for working with atoms, *J. Phys.: Condens. Matter*, 2017, **29**(27), 273002.
36 X. Wang, *XEspresso*, 1.5.1 ed., GitHub repository, 2022.
37 H. J. Monkhorst and J. D. Pack, Special points for Brillouin-zone integrations, *Phys. Rev. B*, 1976, **13**(12), 5188–5192.
38 M. Kawamura, Y. Gohda and S. Tsuneyuki, Improved tetrahedron method for the Brillouin-zone integration applicable to response functions, *Phys. Rev. B*, 2014, **89**(9), 094515.
39 S. J. Pennycook and P. D. Nellist, *Scanning Transmission Electron Microscopy: Imaging and Analysis*, Springer Science & Business Media, 2011.
40 Z. Sun, R. Ahuja, S. Li and J. M. Schneider, Structure and bulk modulus of M2AlC (M=Ti, V, and Cr), *Appl. Phys. Lett.*, 2003, **83**(5), 899–901.
41 B. Stelzer, X. Chen, P. Bliem, M. Hans, B. Volker, R. Sahu, *et al.*, Remote Tracking of Phase Changes in Cr2AlC Thin Films by In-situ Resistivity Measurements, *Sci. Rep.*, 2019, **9**, 7.
42 J. M. Schneider, B. Hjörvarsson, X. Wang and L. Hultman, On the effect of hydrogen incorporation in strontium titanate layers grown by high vacuum magnetron sputtering, *Appl. Phys. Lett.*, 1999, **75**(22), 3476–3478.
43 D. D. Sun, Q. K. Hu, J. F. Chen and A. G. Zhou, First Principles Calculations of the Relative Stability, Structure and Electronic Properties of Two Dimensional Metal Carbides and Nitrides, *Key Eng. Mater.*, 2014, **603**, 527–531.
44 Y.-P. Chien, S. Mráz, M. Fekete, M. Hans, D. Primetzhofer, S. Kolozsvári, *et al.*, Deviations between film and target

compositions induced by backscattered Ar during sputtering from M2-Al-C (M = Cr, Zr, and Hf) composite targets, *Surf. Coat. Technol.*, 2022, **446**, 128764.

45 J. Etzkorn, M. Ade and H. Hillebrecht, V2AlC, V4AlC3-*x* ($x \approx$ 0.31), and V12Al3C8: Synthesis, Crystal Growth, Structure, and Superstructure, *Inorg. Chem.*, 2007, **46**(18), 7646–7653.

46 C. Hu, J. Zhang, J. Wang, F. Li, J. Wang and Y. Zhou, Crystal Structure of V4AlC3: A New Layered Ternary Carbide, *J. Am. Ceram. Soc.*, 2008, **91**(2), 636–639.

47 D. Wang, J. Si, S. Lin, R. Zhang, Y. Huang, J. Yang, *et al.*, Achieving Macroscopic V4C3T*x* MXene by Selectively Etching Al from V4AlC3 Single Crystals, *Inorg. Chem.*, 2020, **59**(5), 3239–3248.

48 X. He, Y. Bai, C. Zhu, Y. Sun, M. Li and M. W. Barsoum, General trends in the structural, electronic and elastic properties of the M3AlC2 phases (M = transition metal): A first-principle study, *Comput. Mater. Sci.*, 2010, **49**(3), 691–698.

49 W. Sailuam, I. Fongkaew, S. Limpijumnong and K. Phacheerak, A first principles investigation on the structural, elastic, and mechanical properties of MAX phase M3AlC2 (M= Ta, Ti, V) as a function of pressure, *Comput. Condens. Matter*, 2022, **30**, e00638.

50 M. Dahlqvist, B. Alling and J. Rosén, Stability trends of MAX phases from first principles, *Phys. Rev. B*, 2010, **81**(22), 220102.

51 P. J. Pöllmann, D. Bogdanovski, S. Lellig, P. Schweizer, M. Hans, C. Azina, *et al.*, Metastable phase formation of (Mo, Cr)2AlB2 MAB phase thin films revealed by theory and experiments, *Mater. Res. Lett.*, 2024, **12**(1), 58–66.

52 M. L. Odlyzko and K. A. Mkhoyan, Identifying Hexagonal Boron Nitride Monolayers by Transmission Electron Microscopy, *Microsc. Microanal.*, 2012, **18**(3), 558–567.

53 P. H. Mayrhofer, D. Music and J. M. Schneider, Influence of the Al distribution on the structure, elastic properties, and phase stability of supersaturated $Ti_{1-x}Al_xN$, *J. Appl. Phys.*, 2006, **100**(9), 094906.